The Astronomical Journal, 159:230 (11pp), 2020 May https://doi.org/10.3847/1538-3881/ab8630

A Single-chord Stellar Occultation by the Extreme Trans-Neptunian Object (541132) Leleākūhonua

Marc W. Buie[1], Rodrigo Leiva[1], John M. Keller[2], Josselin Desmars[3,4], Bruno Sicardy[5], JJ Kavelaars[6], Terry Bridges[7], Robert Weryk[8], Dave Herald[9,10,11], Sean L. Haley[2], Ryder Strauss[2], Elizabeth Wilde[2], Robert Baker[12,13], Ken Conway[12,14], Bryan Dean[12], Mackenzie Dunham[15,16], James J Estes[12,17], Naemi Fiechter[12,16], Rima Givot[12,18], Cameron Glibbery[15,16], Bruce Gowe[15,16], Jennifer N. Hayman[15,16], Olivia L Ireland[15,16], Matthew Kehrli[12,19], Erik M. Moore[15,16], Matthew A. MacDonald[15,16], Delsie McCrystal[12,18], Paola Mendoza[12], Bruce Palmquist[12,20], Sherry Rennau[12,21], Ramsey Schar[12,18], Diana J. Swanson[12,19], Emma D. Terris[15,16], Holly Werts[12], and J. A. Wise[12,13]
[1] Southwest Research Institute, 1050 Walnut St., Suite 300, Boulder, CO 80302, USA; buie@boulder.swri.edu
[2] University of Colorado Boulder, 2000 Colorado Ave, Boulder, CO 80309, USA
[3] Institut Poytechnique des Sciences Avancées IPSA, 63 Boulevard de Brandebourg, F-94200 Ivry-sur-Seine, France
[4] Institut de Mécanique Céleste et de Calcul des Éphémérides, I MCCE, Observatoire de Paris, PSL Research University, CNRS, Sorbonne Universités, UPMC Univ. Paris 06, Univ. Lille, 77 Av. Denfert-Rochereau, F-75014 Paris, France
[5] LESIA, Observatoire de Paris, PSL Research University, CNRS, Sorbonne Université, UPMC Univ. Paris 06, Univ. Paris Diderot, Sorbonne Paris Cité, France
[6] National Research Council of Canada, Victoria BC V9E 2E7, Canada
[7] Dept of Physics and Astronomy, Okanagan College, Kelowna, BC, Canada
[8] University of Hawaii, Manoa, USA
[9] Occultation Section of the Royal Astronomical Society of New Zealand (RASNZ), P.O. Box 3181, Wellington, New Zealand
[10] International Occultation Timing Association (IOTA), P.O. Box 7152, Kent, WA 98042, USA
[11] Canberra Astronomical Society, Canberra, ACT, Australia
[12] RECON, Research and Education Collaborative Occultation Network, USA
[13] Wildwood Institute for STEM Research and Development, Los Angeles, CA, USA
[14] Foothills Library, Yuma, AZ, USA
[15] CanCON, Canadian Research and Education Collaborative Occultation Network, Canada
[16] Penticton Secondary School, Penticton, British Columbia, Canada
[17] Laughlin HS/Bullhead City, Laughlin, NV, USA
[18] Sisters High School, Sisters, OR, USA
[19] California Polytechnic State University, San Luis Obispo, CA, USA
[20] Central Washington University, Ellensburg, WA, USA
[21] Parker High School, Parker, AZ, USA
Received 2019 June 12; revised 2020 March 16; accepted 2020 April 1; published 2020 April 23

Abstract

A stellar occultation by the extreme large-perihelion trans-Neptunian object (541132) Leleākūhonua (also known by the provisional designation of 2015 TG_{387}) was predicted by the Lucky Star project and observed with the Research and Education Collaborative Occultation Network on 2018 October 20 UT. A single detection and a nearby nondetection provide constraints for the size and albedo. When a circular profile is assumed, the radius is $r = 110^{+14}_{-10}$ km, corresponding to a geometric albedo $p_V = 0.21^{+0.03}_{-0.05}$, for an adopted absolute magnitude of $H_V = 5.6$, typical of other objects in dynamically similar orbits. The occultation also provides a high-precision astrometric constraint.

Unified Astronomy Thesaurus concepts: Trans-Neptunian objects (1705); Detached objects (376); Stellar occultation (2135); Astrometry (80)

Supporting material: data behind figures

1. Introduction

The recently discovered trans-Neptunian object (TNO) Leleākūhonua is a dynamically interesting object that is in one of the more extreme outer solar system orbits known so far (Sheppard et al. 2019). Leleākūhonua has an absolute magnitude of $H_V \sim 5.6$ that places it in the top 10% of all TNOs and Centaurs and in the top 20% of all scattered-disk objects in absolute magnitude. Its osculating orbit at the occultation epoch had a semimajor axis of 1019 au and an eccentricity of 0.936, giving it a perihelion distance of 65 au, aphelion distance of 1972 au, orbital inclination of $11\overset{\circ}{.}7$, and orbital period of more than 32,500 yr. The most interesting aspect of the orbit is its perihelion distance, which places it well beyond all of the known perturbers in the solar system. This object is similar in orbital properties to Sedna, another large-perihelion distance object ($a = 479$ au, $e = 0.841$, $i = 11\overset{\circ}{.}9$, $q = 76$ au).

Leleākūhonua is currently faint, but still within reach of large telescopes at a magnitude of $V = 24.6$ at a heliocentric distance of 78.5 au. At aphelion, this object would be all but undetectable at magnitude $V = 38$. Little is known about this object (Sheppard et al. 2019), but the absolute magnitude provides a size constraint. A 4% albedo would imply a diameter of 510 km, while a 30% albedo would imply a diameter of 180 km, where the range is motivated by the albedo estimates of known TNOs (Kovalenko et al. 2017). Despite only having a 3 yr astrometric observational arc at the time of occultation, its positional error was low enough to make it a viable target for study via stellar occultation.

2. Observations

The observations for this occultation campaign were part of the Research and Education Collaborative Occultation Network

(RECON) project (Buie & Keller 2016) in collaboration with the Lucky Star project (see Bérard et al. 2017; Leiva et al. 2017; Ortiz et al. 2017). At the time of the event, the cross-track uncertainty was 8000 km (0.″14), the 1σ timing uncertainty was 5 minutes, and the probability of success was estimated to be 9% based on the RECON prediction and participation by all teams. The network covered from -0.11σ to 0.09σ in the cross-track direction. In the down-track direction, we planned to cover $\pm 2.5\sigma$ (30 minutes). Normal operations for RECON require a 30-day notice for a full campaign, but the notification for this event was too late. In this case, we put out an optional call—meaning teams were encouraged to observe at their discretion. With a cross-track uncertainty of $\pm$8000 km, no particular spot on Earth was preferred, even though our network straddled the predicted centerline. Any site able to see the target star was a useful observing station.

The Lucky Star prediction for the event had a geocentric mid-time of 2018 October 20, 05:08:02 UTC. The RECON prediction had a later mid-time of 2018 October 20, 05:22:31 UTC, a difference of almost 3σ. This difference arises from the astrometry weighting scheme used by Lucky Star (Desmars et al. 2015) compared to RECON, where they give the same weight to all astrometric data (Buie & Keller 2016). We chose to base our observations plan on the RECON prediction because time was short and all the planning information was already available in a form usable by our teams. The RECON prediction (dashed line with gray shading) and the participating sites are shown in Figure 1. The color coding of the event sites uses dark red to indicate a positive detection, blue for data that show no events, and gray for sites that tried but were unable to collect constraining data either positive or negative (additional details are provided in Table 1).

At the time of the event, the object was 78.7 au from the Sun and 77.7 au from the Earth. The TNO was moving 24.0 km s^{-1} on the sky relative to the star (1.5 arcsec hr^{-1}). The sky-plane image scale was 56,000 km arcsec^{-1}. The Gaia DR2 (Brown et al. 2018) position of the star at the epoch of the appulse corrected for parallax was R.A. = 00:12:17.891651, decl. = +13:15:07.49674, and J2000 (Gaia DR2 source ID 2767694522024100608). The uncertainty in the star position, dominated by the proper motion uncertainty, was (0.33, 0.31) mas. These uncertainties include the estimated systematic uncertainties for the parallax and proper motion from Lindegren et al. (2018), which we add in quadrature. The star has a catalog magnitude of $G = 14.5$. For this event, essentially all of the ground-track uncertainty was from the uncertainty in the orbit of the object. At the time of observation, the 81% illuminated Moon was just 36° away from the target star. The Sun was well below the horizon for all teams, ranging from 41° to 54° below the local horizon across the network. The target altitude was high enough, ranging from 52° to 69° above the horizon, for atmospheric attenuation not to be a concern.

Fourteen of the RECON stations attempted the event and of these, ten collected constraining data. From the other four sites, one had telescope alignment issues, two were not able to point to the correct field, and one recorded data only during a portion of the planned time window and started too late. The weather was bad in the middle of the network, preventing any observations there. The observational details are summarized in Table 1. Each entry in the table indicates the team ID, summarized in Buie & Keller (2016) and cross-referenced in

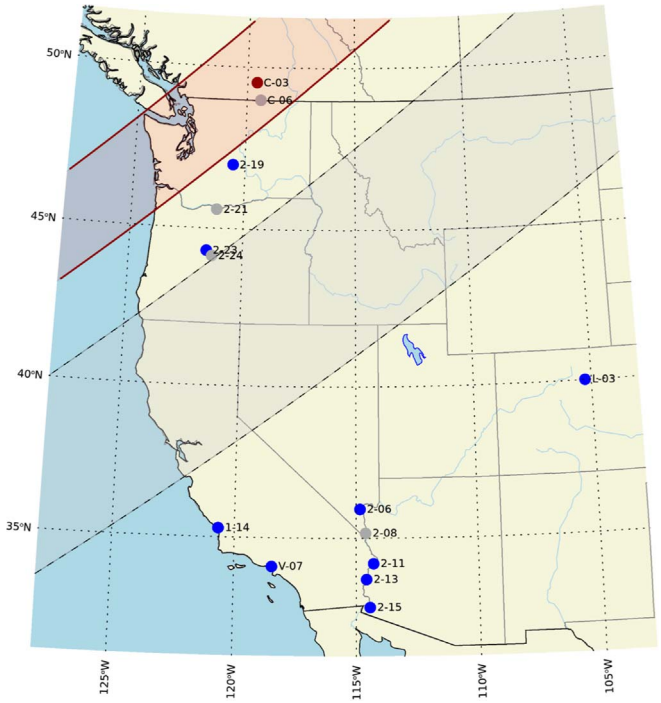

Figure 1. Map showing locations of observing stations and ground-tracks. The labeled symbols indicate the positions of the observations (see Table 1 and Figure 2 for more information about the sites and their data). The pair of dashed lines with the gray shaded region shows the RECON prediction using a diameter of 480 km (5% albedo). The pair of red lines with red shading indicates the actual track and the derived diameter of 220 km (see Section 4). The prediction uncertainty was much too large to be shown on this map.

Figure 2. Note that the "C" codes are for new teams recently added to the network that are sited in southern British Columbia, Canada. The start and ending times of the data recordings are listed. If no times are listed, that team was unable to collect data. The column labeled "SUP" gives the camera "sense-up" setting, roughly equal to an exposure time of SUP/60 s; see Buie & Keller (2016) for details on sense-up. The entries listed for the Canadian sites are actual exposure times. The Canadian sites do not use the standard detector-telescope setup described in Buie & Keller (2016) and can directly set a specific exposure time. The observing locations are then given with the latitude and longitude (in degrees) and the altitude (in meters) on the WGS84 datum. The "Q" column is an indication of the data quality. Those without data recorded but workable sky conditions are shown with 0. The range of 1–5 gives the quality ranging from 1 (lowest) to 5 (best). The observers involved are listed followed by relevant comments regarding the data.

The Canadian sites use a different camera from the other RECON sites (described in Buie & Keller 2016). The new camera is a QHY174M-GPS (hereafter referred to as QHY). This device is based on an sCMOS detector with 1920 by 1200 pixels and a 1 ms readout time and has no mechanical shutter. The images from the QHY cameras were stored directly as FITS image files, unlike the video capture data from the usual RECON systems. More importantly, this new camera has an integrated GPS receiver and the starting times of each image, good to better than 1 ms, are stored with each frame. Penticton (C-03) used a Meade LX200 30 cm $f/10$ reduced to $f/6.3$, giving an effective scale of 0.″7 pixel^{-1} (camera binned 2×2) and a field of view of

Table 1
Participating Sites

SiteID	UT start	UT end	SUP	Lat	Lon	Alt	Q	Observers	Comment
1-14 CPSLO	05:07:35	05:37:44	128	+35.300508	−120.659893	84	3	D. Swanson, M. Kehrli	
2-06 Searchlight	05:07:05	05:37:00	128	+35.965350	−114.836775	695	5	C. Wiesenborn	
2-08 Laughlin	05:07:15	05:37:13	128	+35.162658	−114.610642	251	1	J. Estes, M. Cordero, D.L. Estes, M. Cruz, A, Magaw	Wrong field recorded.
2-11 Parker	05:07:03	05:37:08	128	+34.141088	−114.288362	98	5	S. Rennau, R. Reaves	
2-13 Blythe	05:07:18	05:37:20	128	+33.607967	−114.577870	51	5	D. Barrows, N. Patel	
2-15 Yuma	05:07:11	05:37:20	128	+32.659458	−114.436203	65	4	K. Conway, D. Conway	Vibrations in first 4 minutes.
2-19 Ellensburg	05:05:10	05:30:04	128	+47.002200	−120.540112	489	3	B. Palmquist, R. Palmquist	Vibrations during the capture.
2-21 The Dalles	⋯	⋯	⋯	(+45.596173)	(−121.188597)	(77)	0	B. Dean, M. Dean	Technical issues.
2-23 Sisters	05:07:02	05:37:15	128	+44.296303	−121.577402	968	4	D. McCrystal, R. Schar, R. Givot, P. Mendoza, H. Werts, K. Werts	
2-24 Bend	05:07:04	05:37:42	128	+44.132702	−121.331668	974	1	L. Matheny. A.-M. Eklund, R. Crawford.	Wrong field recorded.
C-03 Penticton	05:05:00	05:37:55	4	+49.533883	−119.557500	470	5	B. Gowe, M. Dunham, J. Hayman, M. MacDonald, E. Moore, N. Fiechter	
C-06 Anarchist	05:15:45	05:33:11	0.5	+49.008827	−119.362968	1087	5	P. Ceravolo, D. Ceravolo	Recording started late.
L-03 SwRI	05:06:14	05:35:25	128	+40.003602	−105.262798	1642	3	J. Keller, R. Leiva, L. Wilde, R. Strauss, S. Haley	
V-07 Wildwood	05:07:01	05:40:31	90	+34.033833	−118.451282	24	4	I. Turk, T.-D. Brown, I. Norfolf, R. Baker, J. Wise	Camera working abnormally.

Note. All site locations are referenced to the WGS84 datum. Positions for sites with no data report the nominal team location (shown with enclosed parentheses) and the team leader(s). The entries in SUP column for C-03 and C-06 are actual exposure times in seconds.

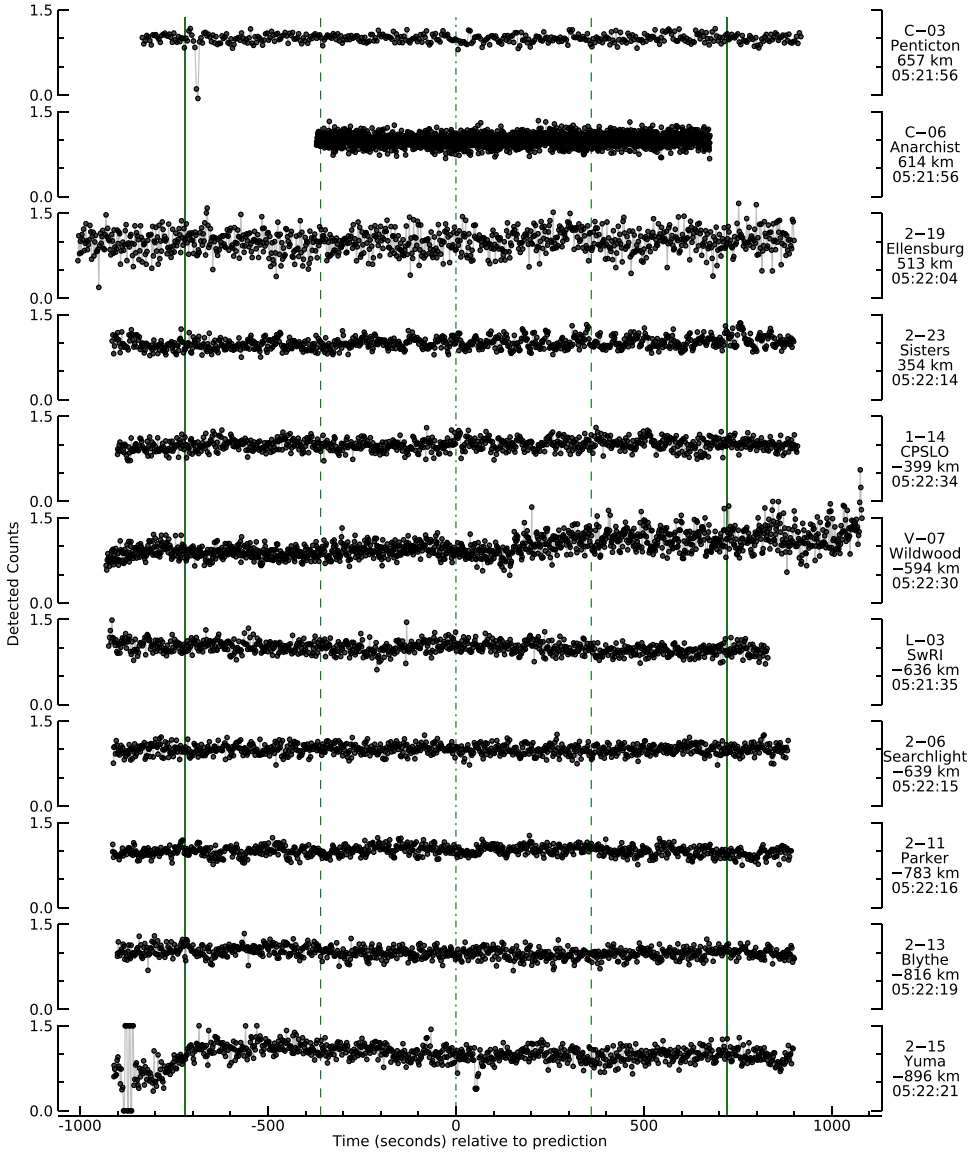

Figure 2. Observations from the 2018 October 20 occultation. The figure shows the light curves from the data collected by the RECON stations. Each subplot is labeled on the right with the team name, cross-track offset, and predicted event time. The plots are all normalized to unit flux when the star is visible. The green vertical lines indicate the predicted 2σ uncertainty limits for the event. An electronic copy of the data in this figure is provided. Uncertainties are included in the electronic data, but are not shown in the plot for clarity.

(The data used to create this figure are available.)

$11\farcm6 \times 7\farcm2$. Image capture was made with SharpCap software version 3.1.5214, using a software gain = 360, which gives an effective gain of 0.116 e^- ADU^{-1} and readout noise of 2.5 e^-. Anarchist Mt. Observatory (C-06) site uses a 30 cm $f/4.9$ Cassegrain astrograph telescope, giving a scale of $0\farcs8$ $pixel^{-1}$ and a field of view of $26\farcm3 \times 16\farcm5$. Image capture was made with SharpCap software version 3.1.5220.0 using a software gain = 400, which gives an effective gain of 0.067 e^- ADU^{-1} and readout noise of 2.3 e^-.

Despite the sparse coverage from the participating sites and the large uncertainty, a positive occultation detection was recorded at Penticton (C-03) with an additional nearby miss at Ellensburg (2–19). Given the site locations involved, the probability of obtaining one or more chords was 6%, and there was an equal chance of obtaining just one chord compared to obtaining multiple chords.

3. Data Analysis

The extraction of timing and light-curve data depends somewhat on the type of system used. Details regarding the RECON video systems can be found in Buie & Keller (2016) and Benedetti-Rossi et al. (2016). In the latter reference, the most relevant information is in Section 3.1.2. All of the data sets other than Penticton (C-03) and Anarchist Mountain Observatory (C-06) were taken with the standard RECON video-based system. The Wildwood (V-07) system is very similar to the standard, but was not provided as a package of gear from RECON. Instead, the Wildwood team procured their own equipment when they joined the project, and it is not precisely the same as the original. As a result, the Wildwood data required additional analysis due to a higher level of variable background video noise. The resulting light curves are

shown in Figure 2, and the details of the data reduction process is given below.

3.1. Video Data

The video processing starts with extraction of time from the IOTA-VTI timestamps superimposed on each video field. Second, the video field order is determined so that the correct video frames are assembled. The integration boundaries are then identified and the sets of frames are averaged to a single image per integration with an integration mid-time determined from the timestamps (see details in Benedetti-Rossi et al. 2016; Buie & Keller 2016). The images have a dark + bias image subtracted in this process. At this point, the series of images is processed with standard image analysis methods.

3.2. sCMOS Imager Data

The Penticton (C-03) and Anarchist Mt. Observatory (C-06) teams used a new model of sCMOS camera, the QHY174M-GPS that was first used for the occultation results on (486958) Arrokoth (Buie et al. 2020), and from that experience, we recommended the Canadian extension (dubbed CanCON) use the QHY camera instead of the current MallinCAM video camera. The processing is much simpler than for video data because the direct product of data collection is to write a series of FITS images, one per integration. These cameras have no appreciable dark current when operated with their cooler set to 0°C or less. The readout bias level has a very stable mean value with structured noise superimposed. The consequence of this is that any image that is read-noise limited has a low-level horizontal banding in the image. This banding has an amplitude of a few counts. We remove this signature from the images by subtracting a robust mean from the image on a row-by-row basis. When complete, the bias, the readout pattern, and the sky have all been subtracted, leaving a mean background of zero. The integration mid-time is then computed from the provided start time and the integration time. At this point, the images are ready for the standard analysis.

3.3. Light-curve Extraction

These images were all processed with aperture photometry methods described in Buie & Bus (1992). For each image, an object aperture radius is selected along with an inner and outer sky annulus radius that optimizes the signal-to-noise ratio (S/N). The apertures were adjusted somewhat between sites, driven by variations in image quality either due to seeing, wind shake, or poor focus. The three radii, in pixels, are give here for each station: Penticton (6, 20, 100), Anarchist Mt. Observatory (4, 20, 100), Ellensburg (10, 20, 100), Sisters (3, 20, 100), CPSLO (4, 20, 100), Wildwood (5, 15, 100), SwRI (4, 20, 100), Searchlight (4, 20, 100), Parker (3, 20, 100), Blythe (4, 20, 100), and Yuma (4, 20, 100). The resulting light curves are shown in Figure 2. In the figure, all of the light curves have been adjusted in time to be relative to the predicted mid-time of the event based on the RECON prediction. Each point in the graph corresponds to a single image. The light curves are ordered by cross-track distance so that the most northerly stations are at the top. The cross-track uncertainty range covered relative to the RECON prediction was from $+0.08\sigma$ to -0.11σ.

3.4. Special Cases

The data from a few of the stations required some extra handling. The deviations from standard processing are summarized in this subsection.

Penticton (C-03): The team did not turn on the cooler for its camera, requiring them to take calibration dark images. These dark calibration data were used to remove hot pixels. The calibration was not ideal because the sensor temperature was unregulated during the capture. However, this did not appear to compromise the occultation result in any measured way.

Ellensburg (2–19): There was an issue with the images where all sources appeared elongated. The observers reported vibration on the observing platform, and the data show precisely the same elongation amount and direction throughout the entire video. We compensated for this problem by increasing the photometry aperture size. There was also light haze at this site, and with the nearby Moon, there was a higher sky background level. All of these conditions conspired to elevate the noise level in these data. Some short dropouts are seen in this light curve, but in all cases, the target star is still seen in the image during the dropouts.

Wildwood (V-07): These data are plagued with issues that could not be fully resolved. The plot in Figure 2 shows a change in the noise properties just after the mid-point of the observing sequence. The team noted the use of SENSEUP = 128, but the data after the noise change appeared to be consistent with an SENSEUP of 90. This latter half of the data is consistent in this regard, but the first half of the data has a variable SENSEUP throughout, starting around 40 and increasing to the value of 90 seen later. This is so mysterious because the possible values of SENSEUP do not include 90, and this is controlled by the camera firmware. There is no way to specify a nonstandard setting. However, we do see a variable SENSEUP after changing this setting, but usually the camera has stabilized to the new value in a minute or two. The constraints provided by this one data set are therefore weaker than would otherwise be the case. These data would show a central chord if present, but sensitivity to grazing chords or small secondary bodies was reduced.

Yuma (2–15): The images were not well focused at the beginning and also showed signs of aberration. This resulted in a slight increase in noise compared to other sites. The dip at the start of the recording seen in Figure 2 is due to the observing team installing a dew shield while collecting data in an attempt to reduce scattered light from the Moon. The dip observed at 5:23 UTC (+50 s relative to prediction) was produced by telescope movements.

4. Results

Inspection of the data revealed an interesting drop out in the Penticton (C-03) data very close to -2σ. No other temporally correlated dips were seen in other data sets. This positive detection is worth a more detailed examination. Figure 3 shows a short segment of the Penticton data around the time 690 s before the nominal RECON prediction. The model curve shown in red is a simple model of a perfectly sharp occultation with start and stop times that are consistent with the fluxes from the light curve at the time of the transitions. Basically, this means that if one point is zero and the next is full flux, then the transition must occur at the edge between the two points. The timing derived from the model occultation curve as shown in

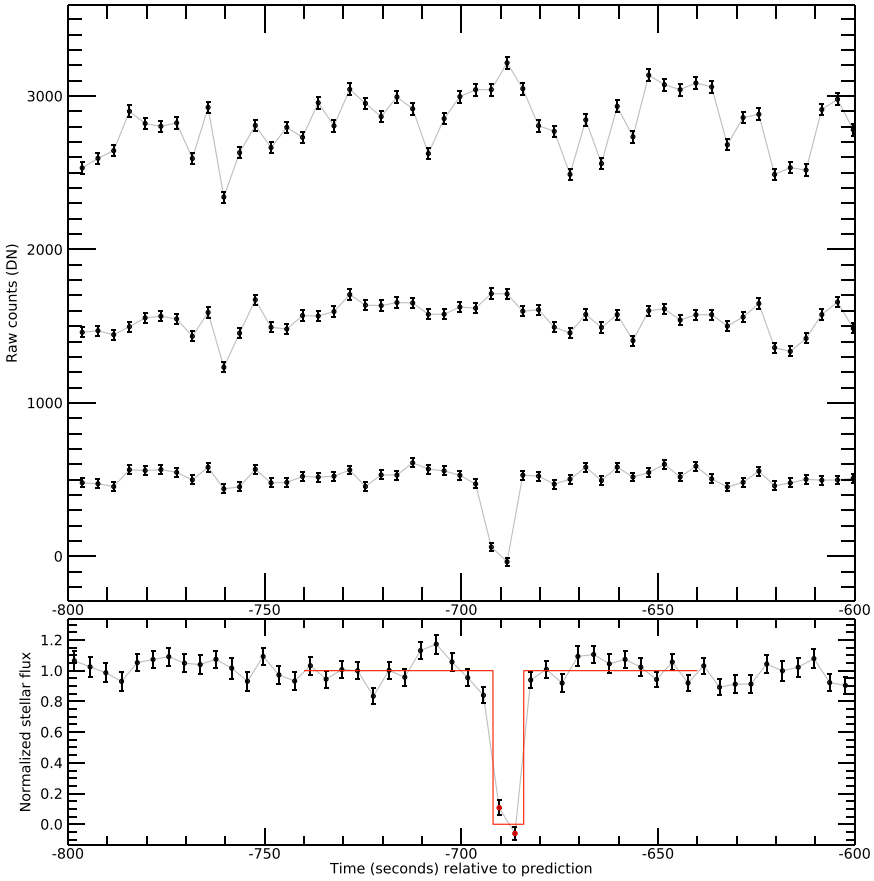

Figure 3. Detailed view of occultation from Penticton (C-03). The top panel shows the raw light curves for the target star (bottom), comparison star 1 (middle), and comparison star 2 (top). The bottom panel shows the ratio of the target star to comparison star 2. This ratio is plotted in Figure 2. The red points highlight the occulted or partially occulted points, and the red curve shows a simple model of the occultation.

Figure 3 is a disappearance at 2018 October 20, 05:10:24.069 UTC and a reappearance at 2018 October 20, 05:10:31.880 UTC. The star was occulted for a total of 7.811 s, equivalent to 187 km given the sky-plane velocity. These timing values are provided for completeness but were not directly used in the diameter determination.

From the Penticton and Ellensburg results, we can place useful constraints on the size of Leleākūhonua even though there was only one measured chord. A Markov chain Monte Carlo scheme is adopted to sample the posterior probability density function (pdf) of the parameters x, y, and r constrained by the light curves with their point-by-point estimated uncertainties. (x, y) is the offset with respect to the ephemeris at the time of the occultation measured in the sky-plane at the distance of the object, and r is the radius of the object. All of the analysis and results here are based on the assumption of a circular profile, and the osculating orbital elements for Leleākūhonua used for the analysis are given in Table 2. No diffraction effects are considered due to the long exposure times and relatively low S/N. Given the large uncertainty in the prediction, the uncertainty in (x, y) prior to the occultation is approximately constant in the relevant zone near Penticton, and it is assumed to have a uniform prior distribution truncated about 2000 km around the main detection. For the radius we consider a power law with slope $q = 4.5$, which is motivated by the power law in the differential size distribution for TNOs with radius $r \gtrsim 50$ km (Bernstein et al. 2004; Fuentes & Holman 2008). The distribution is truncated between

Table 2
Osculating Orbital Elements

Parameter	Value
Epoch	2018 Oct 21 00:00:00 UTC
M	359.337 ± 0.032 (deg)
ω	118.109 ± 0.099 (deg)
Ω	300.868 ± 0.005 (deg)
i	11.662 ± 0.000 (deg)
e	0.937 ± 0.002
a	1018.668 ± 33.042 (au)

Note. Osculating orbital elements for Leleākūhonua used in the analysis. M, ω, Ω, i, e, and a are the mean anomaly, argument of perihelion, ascending node, inclination, eccentricity, and semimajor axis, respectively.

$r_{\rm min} = 50$ km and $r_{\rm max} = 255$ km given by the physically motivated limit in the albedo $0.04 < p_V < 1$.

Figures 4 and 5 provide a graphical summary of the geometry and the astrometric constraints derived from the analysis. The lower left panel in Figure 4 shows the (posterior) joint pdf for the positions x, y in the sky-plane, while the panels in the diagonal are the normalized marginal pdfs for each parameter. The sky-plane is a plane perpendicular to the Earth-star line at the distance of the object with coordinate axes (x, y) in the direction of east and north and with its origin at the ephemeris position of the center of the object (Elliot et al. 1978). The nominal solution is taken from the peak in the

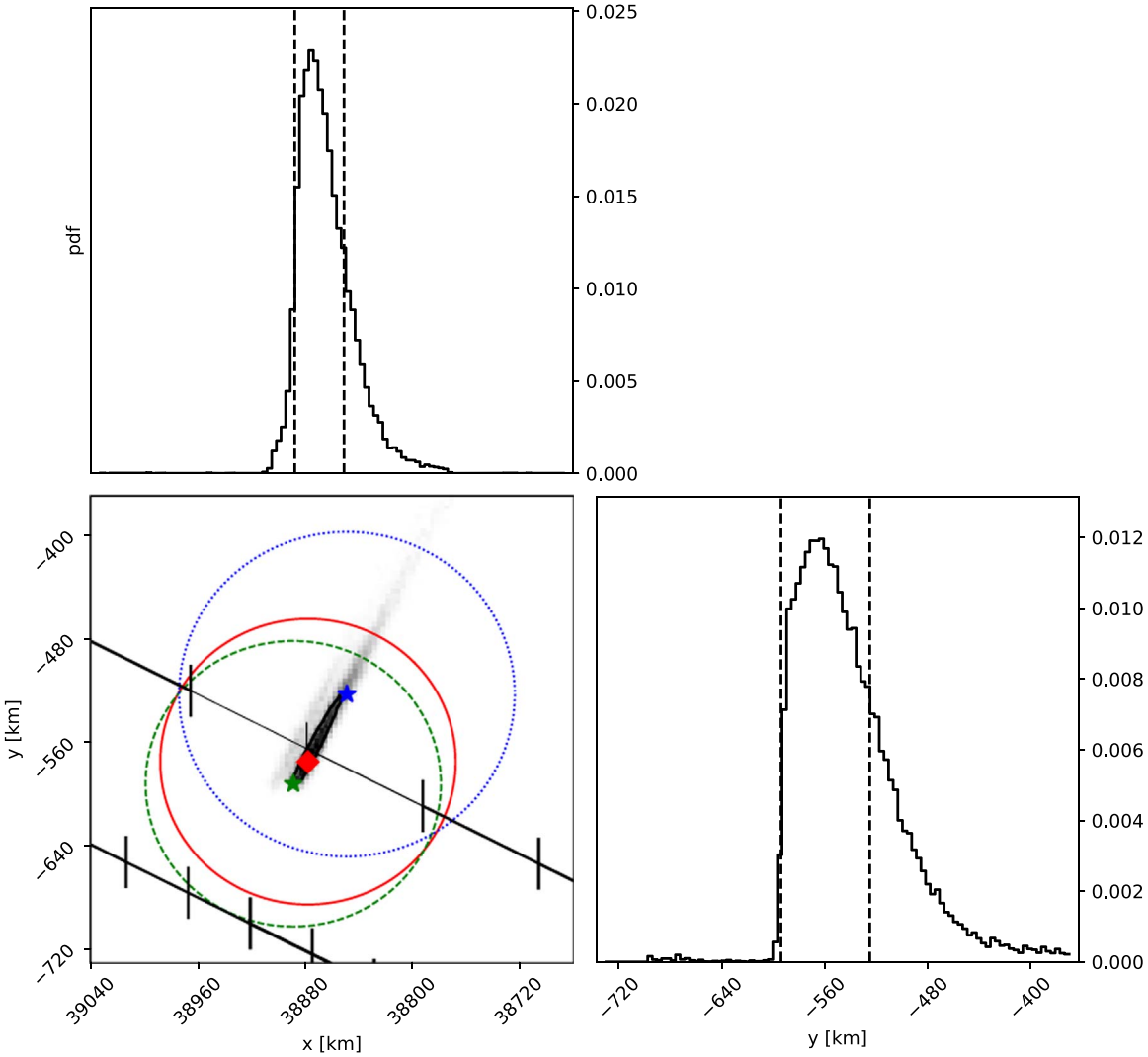

Figure 4. Detailed geometry and constraints from the occultation data. The lower- left panel is the joint pdf for the offset with respect to the adopted object ephemeris in the sky-plane. The contour shows the 39.3% credible interval. The upper and left panels are the normalized marginal pdfs with the 68% credible interval defined with dashed vertical lines. The black segmented lines in the lower left panel show the tracks for Penticton (upper) and Ellensburg (lower), with length representing the exposure time, and the line thickness indicates the normalized flux. The occultation detection is shown with the two central lighter segments. The solid red circle ($D = 220$ km) is the nominal solution for a circular profile centered in the the peak of the marginal pdfs. The center is shown with a diamond, which is the adopted astrometric position of the object at reference time $t_{\rm ref}$. The dashed green circle ($D = 220$ km) and the large dotted blue circle ($D = 250$ km) are the adopted 1σ solutions. The center indicated by star symbols is the intersection of the credible interval shown in the marginal pdfs used to retrieve the astrometric position uncertainties. The astrometric constraints are summarized in Table 3. Note that the joint pdf extends to the upper left corner, whose extreme corresponds to a solution with the imposed limit $p_V = 0.04$ and diameter $D = 510$ km. An electronic copy of the normalized joint pdf in this figure is provided.

(The data used to create this figure are available.)

marginal pdfs. The solid contour in the joint distribution is the 39.3% credible interval, while the vertical dashed lines in the marginal pdfs are the 68% credible intervals and represent the formal 1σ uncertainties. The lower left panel shows the projected locations of the region constrained by the Penticton (upper) and Ellensburg (lower) data. The tracks are computed from the topocentric position of Leleākūhonua as seen from each observing location. The topocentric scale from Penticton at the event mid-time was 56,371.9 km arcsec^{-1}, and the lengths of the segments indicate the exposure time of the data. Superimposed are three illustrative circular profiles compatible with the data, in solid red lines the nominal solution, while the dashed green and dotted blue circles are the two representative 1σ solutions. Given the single detection and the circular profile assumption, there is an expected correlation between the x and y parameters in the cross-track direction. Moreover, the asymmetry in the marginal pdfs is clearly due to the strong negative constraint imposed by the Ellensburg data. Figure 5 shows the positional pdfs projected onto the along-track x_v and cross-track y_c directions. The constraint is tighter in the along-track direction (x_v) with ∼0.2 mas, while the uncertainty in the cross-track direction (y_c) is ∼2 mas.

Each point in the positional pdf implies a size for the object, and the left panel of Figure 6 shows the pdf for the radius r. Of all the priors in our analysis, the most influential on the derived size and albedo of the object is the inclusion of a size distribution. To investigate the sensitivity of our results on the chosen size distribution, we used two additional cases for the priors on the radius. One extreme case is a prior for r with a uniform distribution between 50 and 255 km. The other

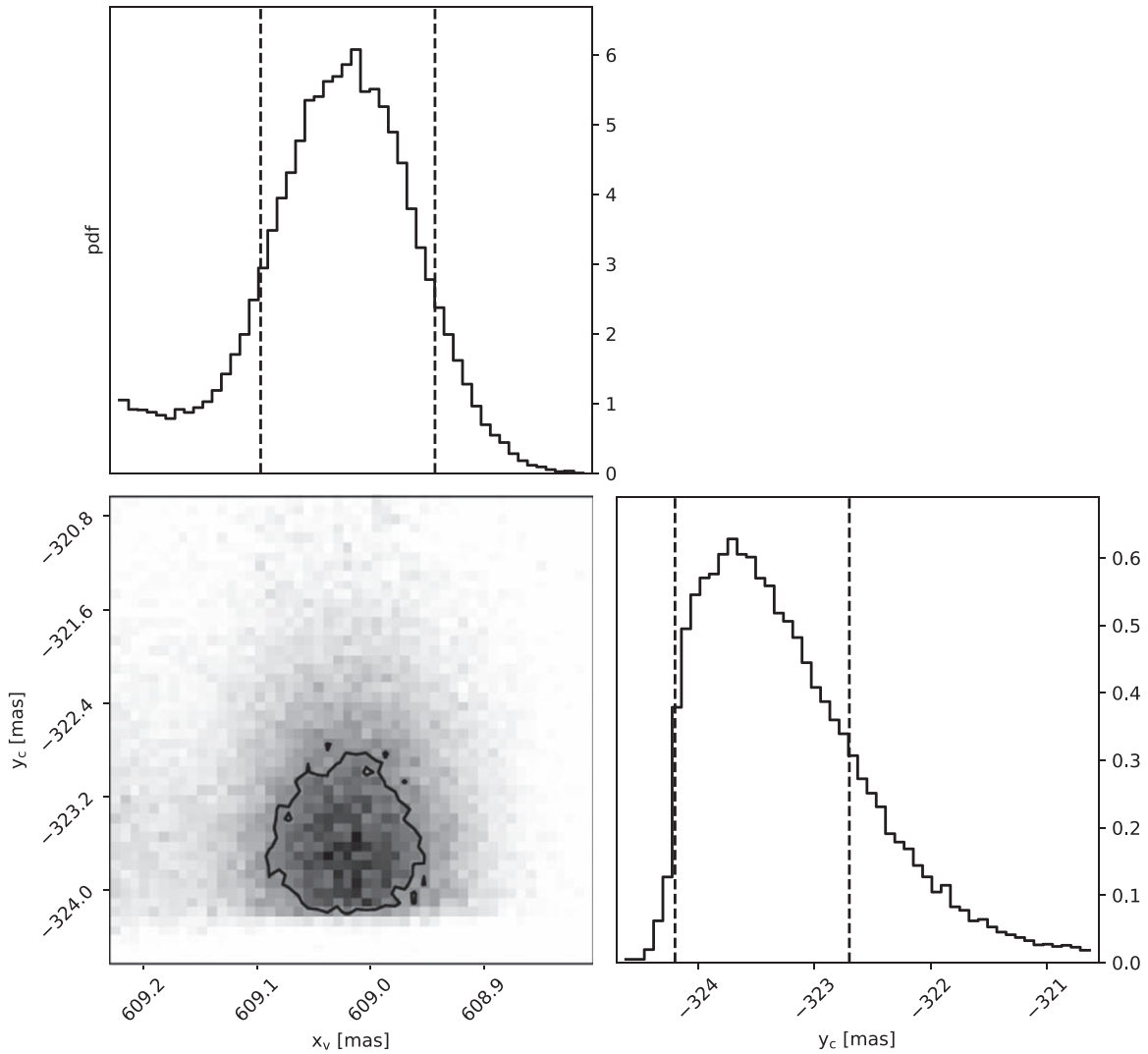

Figure 5. Same pdfs as in Figure 4, but projected in the along-track x_v and cross-track y_c directions and given in milliarcseconds. Contours in the joint pdfs define the 39.3% credible interval. The vertical dashed lines define the 68% credible intervals. From here it is observed that the extended wing in the marginal pdf for the cross-track direction is due to the lack of constraining occultation data north of the Penticton (C-03) site. Note that unlike in Figure 4, the scale of the axes is different and the x_v-axis is stretched with respect to the y_c-axis. An electronic copy of the normalized joint pdf in this figure is provided.

(The data used to create this figure are available.)

extreme case is a significantly steeper power law with slope $q = 7$ that coincides with one of the more extreme slopes suggested for the classical KBO population (Fuentes & Holman 2008). The result from the moderate ($q = 4.5$) power law is shown in black and constrains the object radius to be $r = 110^{+14}_{-10}$ km (vertical dashed lines). The steeper power law ($q = 7$) shown in red is nearly identical to that implied by the moderate power law. The result from the uniform prior on size is shown with the dashed-blue lines and exhibits a long wing in the marginal pdf for larger radii, while the location of the peak in the distribution is essentially the same as in the other two cases. The marginal pdf for the radius r is the main result of our analysis, subject to the validity of the assumption of a circular profile.

The pdf for the size can then be combined with independent measurements of the brightness to retrieve a surface albedo. The right panel of Figure 6 shows a case of the albedo implied by an absolute magnitude of $H_V = 5.6$. For our preferred case of the moderate power law, the albedo is $p_V = 0.21^{+0.03}_{-0.05}$, as indicated by the vertical dashed lines at the $\pm 1\sigma$ locations. The steep power-law case gives nearly identical constraints on albedo. The uniform prior on size shows a bimodal pdf distribution in albedo with significant probability given to a low albedo. We consider the case of a uniform size distribution to be nonphysical. The inclusion of a size distribution is far more reasonable, although the details of which distribution to use is less important to the determination of the albedo than obtaining a more accurate measurement of the absolute magnitude of Leleākūhonua.

Table 3 summarizes the astrometric and physical constraints we derived. The top section of the table shows the nominal radius r and geometric albedo p_V derived from the occultation analysis adopting an absolute magnitude $H_V = 5.6$. The albedo uncertainty does not include any uncertainty from the absolute magnitude. A more complete albedo constraint will come from a better determination of the absolute magnitude of

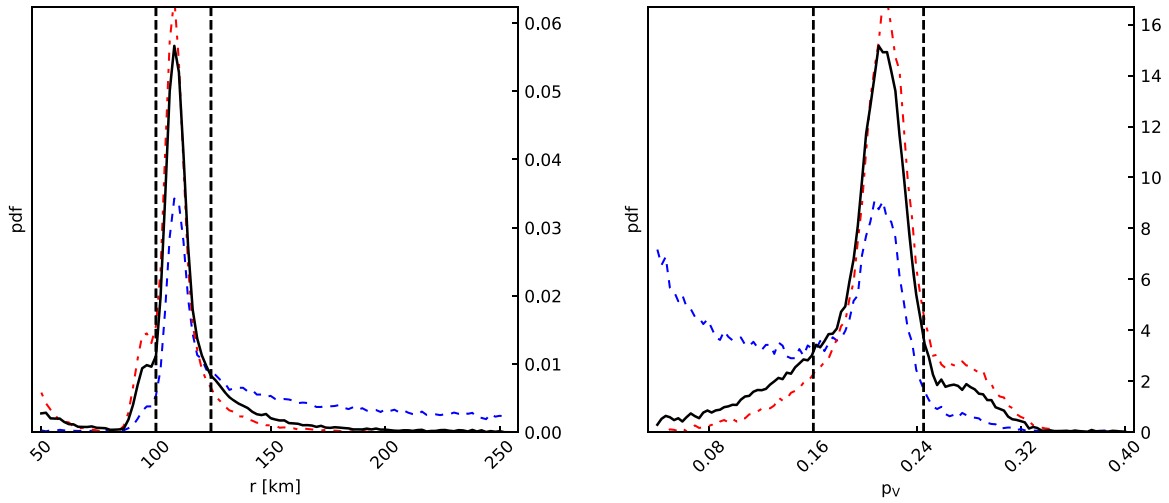

Figure 6. Normalized posterior pdf derived from the occultation analysis comparing different priors for the size distribution. Left: posterior pdfs for the object radius r. Right: derived posterior pdf for the geometric albedo p_V given the adopted absolute magnitude $H_V = 5.6$. The adopted solution is the solid black curve with a truncated power-law distribution for the prior in the radius r with a slope $q = 4.5$. The vertical dashed lines are the 68% credible intervals for the adopted solution. For comparison, the dashed blue lines are the posteriors for a prior in radius r that is uniformly distributed between 50 and 254 km. The dotted red lines are the result of using a power law with a slope $q = 7$. An electronic copy of the marginal pdf for the radius in this figure is provided.

(The data used to create this figure are available.)

Table 3
Astrometric and Physical Constraints

Parameter	Value
Object physical parameters	
r (km)	110^{+14}_{-10}
$p_V(H_V = 5.6)$	$0.21^{+0.03}_{-0.05}$
Reference time and position of the object	
$t_{\rm ref}$	2018 Oct 20 5:22:31.0 UTC
$\alpha_{\rm ref}$	00:12:17.824253
$\delta_{\rm ref}$	+13:15:07.43137
Offset with respect to the object J2000 ephemeris at $t_{\rm ref}$	
$\Delta\alpha\ \cos\delta$ (mas)	$689.7^{+0.2}_{-0.5}$
$\Delta\delta$ (mas)	$-10.2^{+0.9}_{-0.3}$
Offset with respect to the object J2000 ephemeris at $t_{\rm ref}$ in the along-track and cross-track direction	
x_v (mas)	609.0 ± 0.1
y_c (mas)	-323.7 ± 0.8
Offset with respect to astrometric star position	
$\Delta\alpha\ \cos\delta$ (mas)	$-294.4^{+0.2}_{-0.5}$
$\Delta\delta$ (mas)	$-75.6^{+0.9}_{-0.3}$
Object position at $t_{\rm ref}$ derived from the occultation	
α	$00: 12: 17.871489^{+0.2{\rm mas}}_{-0.5{\rm mas}}$
δ	$+13: 15: 07.42118^{+0.9{\rm mas}}_{-0.3{\rm mas}}$

Note. Object position and offset with respect to the astrometric position of the star. $\Delta\alpha\ \cos(\delta)$, $\Delta\delta$ is given in a J2000 coordinate frame. Geometric albedo p_V is based on an adopted absolute magnitude of $H_V = 5.6$.

Leleākūhonua, along with better uncertainties than can be derived from the MPC database. A proper albedo constraint will come from combining our posterior pdf for the size with the results from more complete photometry. For now, our results clearly indicate that the surface has a moderate albedo.

The middle section of Table 3 provides the supporting intermediate values required to compute the final astrometry. From top to bottom, this begins with the reference time and position of the object. The reference time is the time of minimum separation between the star and the object as seen from the geocenter and using the orbit from Table 2. The ephemeris position ($\alpha_{\rm ref}$, $\delta_{\rm ref}$) at that time is also given. Next, the measured offset of the object relative to the ephemeris is given. This value is the numeric result shown graphically in Figure 4. This offset, when rotated to match the direction of motion, gives the cross-track and down-track offsets (x_v, y_c). The nominal values are from the peak in the marginal pdfs, while the uncertainties are from 68% credible intervals. Next, using the ephemeris at the reference time and the astrometric position of the star, the offset with respect to the star is also given. From this final offset, we can then easily compute the astrometric position (α, δ) for Leleākūhonua at the reference time $t_{\rm ref}$ with uncertainties given in mas. These uncertainties do not include the Gaia DR2 positional uncertainty of the star at the epoch of the event and only include our own measurement errors. The astrometric position for Leleākūhonua derived in this work will significantly reduce the uncertainties on future occultation opportunities for this object.

Figure 7 compares the diameter and albedo of Leleākūhonua with other TNOs. The figure shows physical data published through 2018 March from Johnston (2018) and are highlighted based on dynamical class using the DES classification system (Elliot et al. 2005). The pdf from Figure 6 is shown as a black curve for the 1σ region and as a dashed gray curve for the full extension of the pdf. Based on its mostly likely albedo from the pdf, Leleākūhonua has an albedo comparable to other scattered-extended and scattered objects. The average geometric albedo $\overline{p_V}$ for these two dynamical classes in the same size range is 0.17 and 0.20, respectively, and 0.21 and 0.22 when all objects, regardless of diameter, are considered.

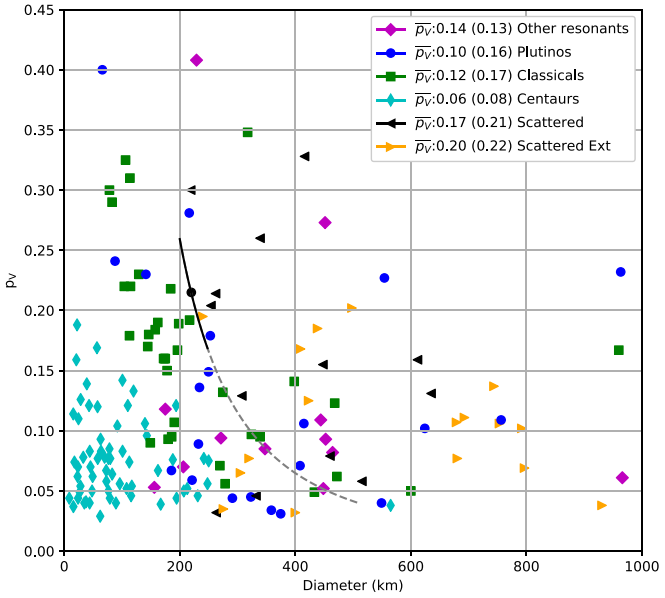

Figure 7. Size and albedo of Leleākūhonua compared to the TNO population. Diameter and albedo are taken from a compilation of values through 2018 March from Johnston (2018). The average value is used for objects with multiple entries. The uncertainties are omitted for clarity. The average geometric albedo $\overline{p_V}$ for objects in the diameter range $200 < D < 500$ km is indicated in the legend. The average geometric albedo is enclosed in parentheses for all the objects in each class, regardless of the diameter. The segmented line is the locus for the adopted absolute magnitude $H_V = 5.6$. The nominal value and uncertainties derived in this work are shown with a black dot and solid line, respectively. The albedo for Leleākūhonua is comparable to that of scattered and scattered-extended objects for the same size range.

5. Conclusions

This first occultation result for Leleākūhonua provides a radius between 100 and 124 km for a circular profile and suggests an albedo in the range of 0.16–0.24. These constraints are the most likely given the occultation data and a typical size distribution of TNOs. The albedo constraint can be improved when better photometry of this object becomes available. The geometric albedo of Leleākūhonua is comparable to that of scattered-extended and scattered objects in the same size range. Given the assumptions in our analysis and given our adopted absolute magnitude, it appears that we can exclude a low albedo. The cumulative probability for the albedo being $\leqslant 5\%$ is 0.004.

Of course, the results of this analysis are subject to the validity of our assumptions. Given the limited data set, it appeared not to be meaningful to investigate a large number of alternative assumptions. Nonetheless, when planning future observations it will be important to recall the assumptions we had to make. Our analysis shows that the choice of size distribution (other than a uniform prior) makes little difference. However, if the object were to have a noncircular profile at the time of this occultation, the change in the inferred albedo would be significant relative to our derived uncertainties of the circular case. If our assumption of a single object is incorrect, it could lead to an even greater change in the derived results. For instance, if this object were actually an equal-size and equal-albedo binary, our data would then apply to just one component and the projected area of the pair would be twice as large, thus implying an albedo that is a factor of two lower. Given our nominal albedo constraint, such a factor of two reduction would still not imply an unrealistic albedo. We have not attempted to calculate the likelihood of these other assumptions, but follow-up occultation observations might well wish to consider the implications of these unconstrained alternative options when a new deployment strategy is set up. All of these questions can be solved with additional occultation observations, preferably with far more than just one positive detection.

These data also provide a new high-precision astrometric constraint that is a factor of 50 better than the positional uncertainty at the time of the occultation. This uncertainty is comparable to the angular size of the body for the high-albedo end of the range and will help pave the way for future occultations with enough chords to obtain a full measure of its shape. For future occultation efforts, we recommend a spacing of no more than 90 km between stations, but tighter spacing will be highly desirable. The spread of stations would need to be much larger than our measured size to be sensitive to a binary object. A second more detailed set of occultation observations can greatly constrain the future interpretation of this occultation result.

Despite the new astrometric constraint, this object will require further astrometric observations to preserve the ability to obtain a high-precision occultation prediction. The new measurement provided here does not appreciably extend the observational arc for this object. As such, it merely provides a very accurate fiducial point for the orbit estimate. The errors in the mean motion will quickly begin to dominate future predictions without further data. New astrometry, even at lower precision than provided by an occultation, will continue to improve on the mean motion just by extending the temporal arc of the data. However, it would be well advised for future astrometrists to obtain high S/N detections. The best astrometry being reported from the ground today, reduced against Gaia DR2 and measured by the post-orbit fit scatter, seems to be good to roughly $0\farcs1$, and more data as good as this (or better) would help greatly. Current data on Leleākūhonua show an rms scatter of $0\farcs17$ with one-third having residuals as large as $0\farcs3$–$0\farcs4$, so there is much room for improvement. We can expect to have future opportunities to learn more about this distant object provided regular high-quality astrometric observations are obtained in addition to new occultation data.

This work is made possible by the people that are part of RECON and CanCON: teachers, students, and other community members, including Toochi Brown, David Bryan Barrows, Ceravolo Anarchist Mt. Observatory, Anna Chase, Dorey Conway, Mark Cordero, Ron Crawford, Maritz Cruz, Michelle Dean, Anne-Marie Eklund, Dawn L. Estes, Kristof Klees, Aundriana Magaw, Lara Matheny, Ian R. Norfolk, Rhonda Palmquist, Nidhi R. Patel, Robert Reaves, Andrew Scheafer, Paul Snape, Ihsan A. Turk, Hunter VandenBosch, Eric Verheyden, Kellen Werts, and Charlene Wiesenborn. The observers listed in the table are but a small fraction of the total network, and their dedication to this project is deeply appreciated. Funding for RECON was provided by a grant from NSF AST-1413287, AST-1413072, AST-1848621, and AST-1212159. Some of the work leading to these results has received funding from the European Research Council under the European Community's H2020 2014-2020 ERC Grant Agreement #669416 "Lucky Star." J.J.K. acknowledges the support of the Natural Sciences and Engineering Research Council of Canada (NSERC) [RGPIN/5499-2016]. T.J.B. acknowledges the support of Okanagan College through the Grants-in-Aid fund. Special thanks to the entire Gaia mission team for their amazing star catalog.

ORCID iDs

Marc W. Buie https://orcid.org/0000-0003-0854-745X
Rodrigo Leiva https://orcid.org/0000-0002-6477-1360
John M. Keller https://orcid.org/0000-0002-0915-4861
Josselin Desmars https://orcid.org/0000-0002-2193-8204
Bruno Sicardy https://orcid.org/0000-0003-1995-0842
JJ Kavelaars https://orcid.org/0000-0001-7032-5255
Robert Weryk https://orcid.org/0000-0002-0439-9341

References

Benedetti-Rossi, G., Sicardy, B., Buie, M. W., et al. 2016, AJ, 152, 156
Bérard, D., Sicardy, B., Camargo, J. I. B., et al. 2017, AJ, 154, 144
Bernstein, G. M., Trilling, D. E., Allen, R. L., et al. 2004, AJ, 128, 1364
Brown, A. G. A., Vallenari, A., Prusti, T., et al. 2018, A&A, 616, A1
Buie, M. W., & Bus, S. J. 1992, Icar, 100, 288
Buie, M. W., & Keller, J. M. 2016, AJ, 151, 73
Buie, M. W., Porter, S. B., Tamblyn, P., et al. 2020, AJ, 159, 130
Desmars, J., Camargo, J. I. B., Braga-Ribas, F., et al. 2015, A&A, 584, A96
Elliot, J. L., Dunham, E., Wasserman, L. H., & Millis, R. L. 1978, AJ, 83, 980
Elliot, J. L., Kern, S. D., Clancy, K. B., et al. 2005, AJ, 129, 1117
Fuentes, C. I., & Holman, M. J. 2008, AJ, 136, 83
Johnston, W. R. 2018, TNO and Centaur Diameters, Albedos, and Densities V1.0, NASA Planetary Data System
Kovalenko, I. D., Doressoundiram, A., Lellouch, E., et al. 2017, A&A, 608, A19
Leiva, R., Sicardy, B., Camargo, J. I. B., et al. 2017, AJ, 154, 159
Lindegren, L., Hernández, J., Bombrun, A., et al. 2018, A&A, 616, A2
Ortiz, J. L., Santos-Sanz, P., Sicardy, B., et al. 2017, Natur, 550, 219
Sheppard, S. S., Trujillo, C. A., Tholen, D. J., & Kaib, N. 2019, AJ, 157, 139